Nanoscale

ROYAL SOCIETY OF CHEMISTRY

MINIREVIEW

View Article Online
View Journal | View Issue

Cite this: *Nanoscale*, 2023, **15**, 998

Generating spin-triplet states at the bulk perovskite/organic interface for photon upconversion

Colette M. Sullivan and Lea Nienhaus *

Perovskite-sensitized triplet–triplet annihilation (TTA) upconversion (UC) holds potential for practical applications of solid-state UC ranging from photovoltaics to sensing and imaging technologies. As the triplet sensitizer, the underlying perovskite properties heavily influence the generation of spin-triplet states once interfaced with the organic annihilator molecule, typically polyacene derivatives. Presently, most reported perovskite TTA-UC systems have utilized rubrene doped with ~1% dibenzotetraphenylperiflanthene (RubDBP) as the annihilator/emitter species. However, practical applications require a larger apparent anti-Stokes than is currently achievable with this system due to the inherent 0.4 eV energy loss during triplet generation. In this minireview, we present the current understanding of the triplet sensitization process at the perovskite/organic semiconductor interface and introduce additional promising annihilators based on anthracene derivatives into the discussion of future directions in perovskite-sensitized TTA-UC.

Received 17th October 2022,
Accepted 12th December 2022

DOI: 10.1039/d2nr05767k

rsc.li/nanoscale

Introduction

The inherent longevity of spin-triplet states[1] makes these uniquely qualified as solar energy storage states prior to utilization. Hence, triplet states can be utilized to extend the photoexcited state lifetime, enabling, for example, efficient

Department of Chemistry and Biochemistry, Florida State University, Tallahassee, FL 32306, USA. E-mail: lnienhaus@fsu.edu

Colette M. Sullivan

Colette M. Sullivan received her B.S. from the University of South Carolina Aiken in 2021. In the Fall of 2021, she joined The Nienhaus group at Florida State University to pursue her graduate degree. Her research interests include exploring photon upconversion in perovskite-sensitized systems using a variety of optical and structural characterization methods.

Lea Nienhaus

Dr. Lea Nienhaus received her B. Sc. in Chemistry from the Universität Ulm, Germany in 2010 and her Ph.D. in Chemistry from the University of Illinois at Urbana-Champaign in 2015 working with Professor Gruebele. Following her postdoctoral work with Professor Bawendi at MIT, she began her independent career at Florida State University in 2018. Current research directions in the Nienhaus lab focus on triplet generation at the hybrid inorganic/organic interface. In particular, emphasis is placed on utilizing bulk perovskite materials as triplet sensitizers for photon upconversion. The utilized combination of optical spectroscopy and scanning probe microscopy enables a unique understanding the complex photophysical processes occurring in these systems.

photocatalysis[2–5] or photon upconversion (UC) at low, solar-relevant fluxes.[6–8]

However, one major drawback of the use of such triplet states is that their direct optical excitation is a spin-forbidden process. Thus, it exhibits a low oscillator strength. To efficiently utilize triplet states for the aforementioned applications, a higher triplet yield is required than can be obtained by direct optical excitation. However, triplet states can also be efficiently populated *via* Dexter-type exchange interactions.[9] Hence, molecules which exhibit efficient intersystem crossing or strong direct singlet-to-triplet absorption due to increased spin–orbit coupling caused by the inclusion of heavy metals can be used to indirectly populate the triplet states of the desired molecules. However, large energy losses of up to 1 eV can be associated with intersystem crossing due to large exchange energies, diminishing their benefit.[10–12] To overcome this energetic hurdle, in 2015, nanocrystals were introduced as triplet sensitizers.[13,14] In contrast to the established molecular approaches for triplet sensitization, in nanocrystals, spin is not a good quantum number due to strong spin–orbit coupling. Rather, the total angular momentum must be considered and as a result, the lowest exciton state has both singlet and triplet character at room temperature. Hence, nanocrystals enable nearly isoenergetic triplet sensitization. While initial studies focused on conventional nanocrystals such as PbS and CdSe, more recently, less conventional nanocrystals including perovskite NCs,[15–18] ternary quantum dots[18] or Si nanocrystals have also been introduced.[19] Depending on the specific system investigated, the spin-triplet states were generated either by a Dexter-type bound triplet energy transfer or a two-step charge transfer process.[20–23] For detailed reviews on photon UC, we refer the readers to the following review articles.[24–29] However, despite these novel and often efficient approaches of generating triplet excitons in organic molecules, a significant hurdle remained: the integration into the solid state.[30] This limitation was, in part, caused by a lack of long-range exciton diffusion in the utilized nanocrystal thin films, which limited the absorbance of the triplet sensitizer.[31]

To overcome this hurdle, bulk perovskite materials with long free carrier lifetimes and diffusion lengths[32–34] and high absorption cross sections[35] were introduced as triplet sensitizers. Triplet exciton generation at the bulk lead halide perovskite/organic semiconductors (OSC) interface was first demonstrated by Nienhaus *et al.* in 2019.[36,37] In contrast to other popular ways to generate bound triplet states in OSC molecules, such as energy transfer from triplet states generated by intersystem crossing in metal–organic complexes[38–41] or from nanocrystals which do not possess a defined spin state,[16,17,42–46] here, the bound spin-triplet state is formed by recombination of free charge carriers at the perovskite/OSC interface.[30,47]

To date, most work on triplet sensitization at inorganic/organic hybrid interfaces has focused on the application of photon UC. In general, photon UC describes a process in which lower energy photons are converted to ones of higher energy, resulting in an apparent anti-Stokes shift in the emission wavelength. To ensure this process complies with energy conservation laws, a minimum of two low energy photons are required to form a single high energy photon. Multiple mechanisms yielding upconverted emission are possible, including second-harmonic frequency generation,[48–50] utilization of the ladder-like energy levels of lanthanide ions[51,52] or triplet–triplet annihilation (TTA),[7,8,36,53] a process in which two triplet states combine to generate a higher energy singlet state in a spin-allowed Dexter-type energy transfer process. For TTA-UC processes, the first step generates a triplet pair state ^{1}(TT) from two triplet states T_1 with a rate k_1, which yields the singlet state S_1 with the rate k_2.

$$T_1 + T_1 \underset{k_{-1}}{\overset{k_1}{\rightleftharpoons}} {}^1(TT) \underset{k_{-2}}{\overset{k_2}{\rightleftharpoons}} S_1 + S_0 \quad (1)$$

Reversal of this process results in singlet fission (SF), which is a competing process for triplet annihilators such as rubrene with triplet energies at half of the singlet energy: $E(T_1) = 0.5E(S_1)$.[13]

A figure of merit for the TTA-UC process is the efficiency Φ_{UC}, which is based on the product of the energy transfer efficiency from sensitizer to annihilator Φ_{TET} and the TTA efficiency Φ_{TTA}. To account for the generally low quantum yields of OSCs in solid state, it is often normalized by the annihilator quantum yield (QY) Φ_{ann}, to deconvolute the effects of the TTA-UC QY and OSC QY:[54]

$$\Phi_{UC} = \Phi_{TET}\Phi_{TTA}\Phi_{ann} \quad (2)$$

In perovskite-sensitized TTA-UC, the perovskite essentially acts as an *in situ* solar cell driving a TTA-based organic light-emitting diode: hole transfer occurs from the perovskite valence band (VB) to the highest occupied molecular orbital (HOMO) of the annihilator while direct electron transfer from the conduction band (CB) to the lowest unoccupied molecular orbital (LUMO) is blocked due to a large energy barrier of around 1 eV.[36] The triplet state, however, is directly accessible by charge transfer, as shown for the perovskite/rubrene interface in Fig. 1a.

One of the major shortcomings of bulk perovskite-sensitized solid-state UC has been that, to date, most studies have focused only on rubrene as the triplet annihilator. Rubrene, the current workhorse of solid-state UC, was initially chosen on account of its known performance in solution-phase[55–57] and solid-state UC.[12,58,59] In addition, its triplet energy sufficiently matched the lead halide perovskite band energy for a proof-of-concept study, and most importantly, the triplet state was energetically accessible by a free charge carrier injection. Yet, the fundamental 0.4 eV energy mismatch between the perovskite band gap and the triplet energy of rubrene (T_1 = 1.14 eV), coinciding with the energy loss during hole transfer (Fig. 1a), introduces a large energy loss, which minimizes the achievable apparent anti-Stokes shift. In addition, since rubrene is both a known TTA-UC and SF material, the QY of rubrene is very low in solid state. Hence, ~1% dibenzotetraphenylperiflanthene (DBP) is commonly doped into the rubrene film to boost the QY at the cost of the achievable apparent anti-Stokes shift.[13] Therefore, the limited energy gain

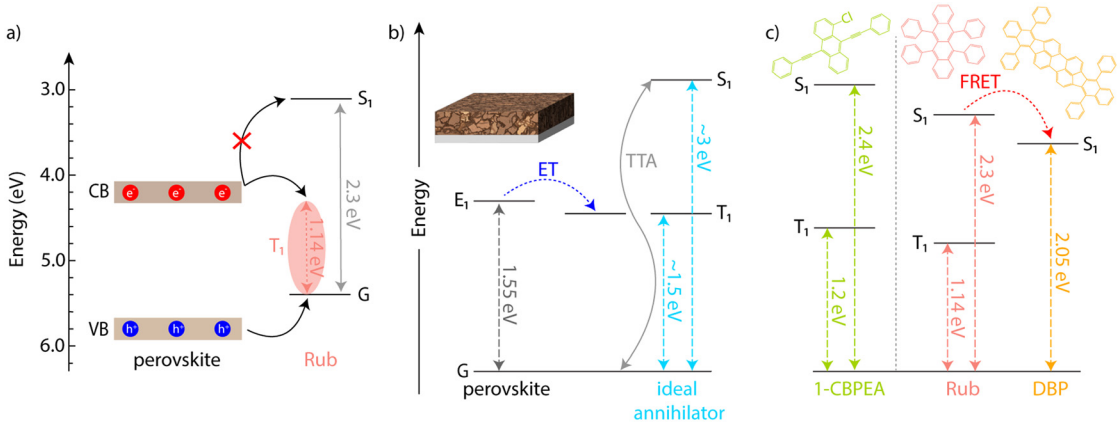

Fig. 1 (a) Perovskite and rubrene energetic alignment. (b) Schematic of perovskite sensitized triplet–triplet annihilation (TTA) upconversion (UC) to an 'ideal annihilator'. Excitation of the perovskite sensitizer results in electron transfer (ET) to the T_1 of the annihilator molecule. TTA occurs upon the interaction of two sufficiently populated annihilators where radiative decay of the S_1 state produces the upconverted photon. (c) Energy levels of 1-CBPEA and RubDBP. An additional energy transfer (FRET) to DBP results in the desired high energy singlet states.

from 800 nm (1.55 eV) to 605 nm (2.05 eV) when using a formamidinium methylammonium lead triiodide ($FA_{0.85}MA_{0.15}PbI_3$, FAMA) sensitizer and rubrene/DBP (RubDBP) is far from optimal. Ideally, the UC process should minimize energy losses during the triplet sensitization process by a well-matched bandgap/triplet energy level $E_{bandgap} \approx E(T_1)$ and maximize the obtained apparent anti-Stokes shift effectively doubling the perovskite bandgap in TTA-UC: $E(S_1) = 2E(T_1)$. We detail this 'ideal annihilator' in Fig. 1b alongside the two annihilators reported to date: RubDBP and 1-chloro-9,10-(bisphenylethynyl)anthracene (1-CBPEA).[60] The true potential of perovskite-sensitized TTA-UC will be accomplished once 800 nm (1.55 eV) incident light is successfully upconverted to ~410 nm (3 eV), thus, maximizing the attainable energy gain obtained in the UC process.

To achieve this goal, novel annihilators must be both compatible in terms of the absolute energy alignment of the perovskite band gap with the triplet state, as well be efficient annihilators in solid state. One of the major drawbacks of solid-state UC are intermolecular interactions between OSC molecules. These interactions can influence the singlet/triplet energy surfaces or result in undesired excimer formation causing low photoluminescence (PL) QYs due to SF or an increase in the nonradiative decay rate.[61–64] Consequently, only few annihilators which exhibit high performance in solution are also viable contenders in solid-state. For example, 9,10-diphenylanthracene is the state-of-the-art annihilator for solution-based green-to-blue or red-to-blue UC.[42–44,65–68] However, excimer formation in the solid state shifts the emission from the desired high energy blue (~2.9 eV) to green (~2.4 eV) and reduces the QY.[69] On the other hand, excimer formation can also be utilized to suppress SF.[70,71] To expand the library of viable annihilators and demonstrate that triplet generation the perovskite/OSC interface is a universal process not inherently limited to the perovskite/rubrene interface, we have recently reported solid-state near-infrared-to-visible UC using a FAMA sensitizer and 1-CBPEA annihilator, which enables UC from near-infrared (800 nm) to green (550 nm) as shown in Fig. 2.[60]

In the following minireview, we will detail the current understanding of the triplet generation mechanism at the perovskite/OSC interface and the resulting implications for photon UC and discuss the current status of the field of perovskite-sensitized TTA-UC. While significant advancements have been made in the fundamental understanding of the charge transfer processes underpinning perovskite-sensitized UC devices over the last few years and device improvements have made by compositional tuning and surface treatments, a key goal moving forward must be to both improve both the UC performance and the apparent anti-Stokes shift.

Mechanistic insights

One of the key factors in expanding and improving the triplet generation at the perovskite/OSC interface is a fundamental understanding of the triplet generation process. We begin this

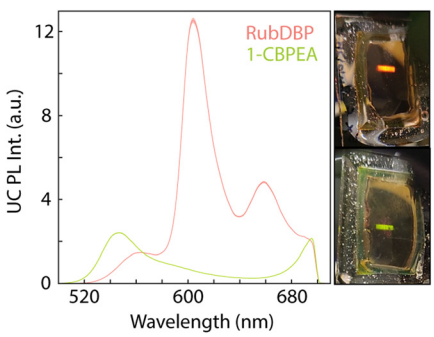

Fig. 2 Upconverted emission of FAMA/RubDBP and FAMA/1-CBPEA bilayer films. Excitation under 780 nm light results in peak emissions at 605 nm (RubDBP) and 550 nm (1-CBPEA). Photos to the side of the corresponding films (top: RubDBP; bottom: 1-CBPEA). Reproduced from ref. 60 with permission from the Royal Society of Chemistry, copyright 2022.

minireview by discussing the current understanding of the mechanism underlying perovskite-sensitized UC.

Due to the low exciton binding energy of lead halide perovskites on the order of ambient thermal energy (kT),[32] the initially photoexcited excitons rapidly evolve into free charge carriers. As a result, a triplet generation mechanism at the perovskite/OSC interface based on a bound exciton transfer is unlikely. In addition, the p-type semiconductor rubrene has been previously investigated as a hole transfer layer for perovskite-based solar cells, indicating efficient hole extraction occurs at the interface.[72–74] Due to the band alignment shown in Fig. 1a, a free charge carrier-based mechanism is expected as shown in Fig. 3a. In the first step, the hole transfers to the HOMO of the OSC. This hole can localize in form of a polaron, and Coulombic interactions can facilitate the desired electron–hole recombination to the bound triplet state.

To understand the mechanism of interfacial charge transfer in detail, the ultrafast kinetics of triplet formation have been investigated at the interface of methylammonium formamidinium lead triiodide ($MA_{0.85}FA_{0.15}PbI_3$, MAFA) and rubrene/1% DBP (MAFA/Rub) by transient absorption (TA) spectroscopy. A major benefit of this approach over PL spectroscopy is the ability to observe the spin-allowed $T_1 \rightarrow T_n$ transition of the triplet state directly. Under 700 nm excitation, lead halide perovskites exhibit two characteristic photobleaches (PBs) in the spectral window investigated.[75–77] The photobleach associated with the ground state bleach (PB1) is found at 780 nm, while a higher energy PB is found at 485 nm. The precise origin of PB2 is still unclear, and has been attributed to multiple effects including a band structure including one shared valence band (VB) and two conduction bands (CBs),[78,79] two VBs and a common CB,[77,79] or a high energy charge transfer (CT) state accredited to an I_2-like species which is formed under illumination.[76] Once the perovskite is interfaced with rubrene, TA spectroscopy reveals the additional rubrene-related photo-induced absorptions (PIAs) at 480 nm, 520 nm, and 550 nm (Fig. 3b).[6,80–83]

Investigation of the underlying perovskite dynamics reveals several key features: (1) a faster population of the perovskite photobleach (PB1) in the presence of rubrene, (2) lower extracted carrier temperatures for the MAFA/Rub bilayer *vs.* MAFA and (3) a faster recovery of PB1 and the correlated photo-induced absorption (PIA1) (Fig. 3c) in the first 20 ps.[8] Unraveling the overlapping rubrene kinetics reveals the emergence of the rubrene triplet photoinduced absorptions for the $T_1 \rightarrow T_n$ and polaron on a sub-nanosecond timescale (Fig. 3d). Taken together, this indicates that carrier extraction at the perovskite/rubrene interface is an ultrafast process involving the extraction of hot carriers.[84–86] This result provides some insight as to why the charge extraction yield is currently still lacking. While hot carriers are rapidly extracted at the surface, charges further away from the interface will be diffusion-limited and will have cooled prior to reaching the interface thus slowing their extraction.

Similarly, comparing the TA spectroscopy for formamidinium methylammonium lead triiodide ($FA_{0.85}MA_{0.15}PbI_3$, FAMA) perovskite bilayers: FAMA/RubDBP (Fig. 4c) and FAMA/1-CBPEA (Fig. 4d), highlights the rapid emergence of the triplet-related excited state absorption (ESA) features for the respective OSCs.[60] Additionally, evidence of SF within both

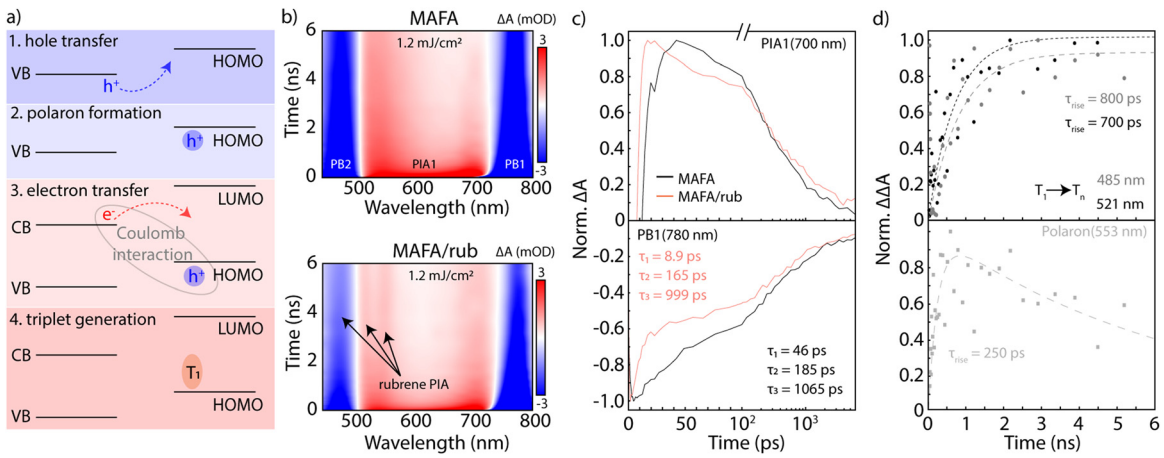

Fig. 3 (a) Mechanistic outline for perovskite-sensitized TTA-UC, beginning with hole transfer from the perovskite valence band (VB) to the highest occupied molecular orbital (HOMO) of the annihilator (step 1). A charged polaron species then forms (step 2), which can Coulombically interact with the electrons in the perovskite conduction band (CB) pulling electrons over to the annihilator (step 3) forming the triplet exciton (step 4). Adapted with permission from ref. 125. Copyright 2022 John Wiley and Sons. (b) Transient absorption maps for MAFA only and MAFA/rub films under 700 nm pump. Perovskite bleach features at 780 nm (PB1) and 485 nm (PB2) and photo-induced absorption (PIA1) are marked. In the bilayer film, additional PIA features from rubrene are labeled. (c) Normalized kinetic traces extracted at 700 nm (PIA1, top) and 780 nm (PB1, bottom) for the MAFA (black trace) and MAFA/rub (pink trace) films. Corresponding decays for the PB1 traces are included in as insets. (d) Normalized traces for the $T_1 \rightarrow T_n$ rubrene transitions (top) at 485 nm (grey) and 521 nm (black) and the polaron PIA at 533 nm (bottom) with the corresponding rise times included. Adapted with permission from ref. 8. Copyright 2022 American Chemical Society. https://doi.org/10.1021/acsenergylett.1c02732. Further permissions related to the material excerpted should be directed to the ACS.

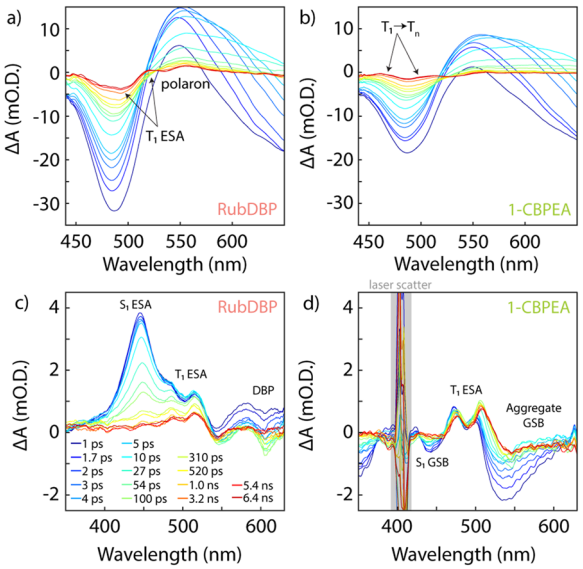

Fig. 4 Absorbance spectra from selected delay times for bilayer (a and b) under 700 nm pump and OSC only films (c and d) under 400 nm pump. (a) Transient absorbance spectra of FAMA/RubDBP bilayer film where the triplet (T_1) excited state absorption (ESA) at 520 nm and polaron signal of rubrene at 550 nm are highlighted. (b) Absorbance spectra of a FAMA/1-CBPEA bilayer film with the $T_1 \rightarrow T_n$ transitions at 460 nm and 510 nm of the 1-CBPEA annihilator shown. (c) RubDBP OSC only absorbance spectra where the singlet (S_1) ESA at 445 nm and T_1 ESA spectral features at 485 nm and 515 nm corresponding to rubrene are observed as well as the DBP bleach at 600 nm. (d) 1-CBPEA OSC absorbance spectra where the S_1 ground state bleach (GSB) at 440 nm and T_1 ESA transitions at 470 nm and 510 nm are observed with an additional bleach feature at 530 nm. Grey box denotes pump laser scatter. Reproduced from ref. 60 with permission from the Royal Society of Chemistry, copyright 2022.

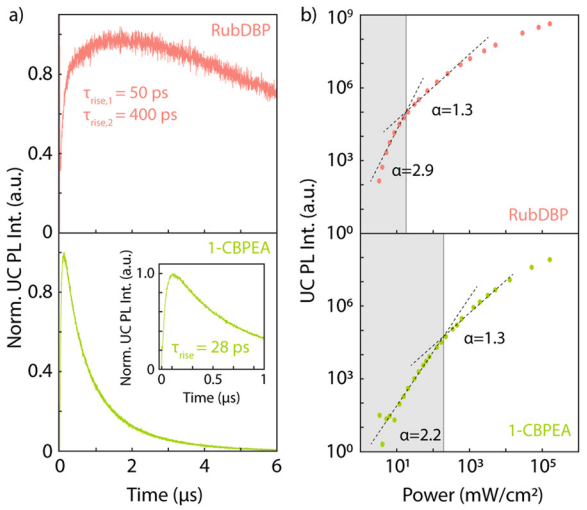

Fig. 5 (a) Normalized upconverted PL dynamics for FAMA/RubDBP (top) and FAMA/1-CBPEA (bottom) bilayer films under 780 nm pulsed excitation (50 kHz, 120 mW cm^{-2}). Extracted triplet rise times are included for both, and smaller inset magnifies the quick rise of 1-CBPEA. (b) Power dependent upconverted emission for both FAMA/RubDBP (top) and FAMA/1-CBPEA (bottom) bilayer films with the corresponding extracted slopes (grey dashed lines) included. The calculated intensity threshold for each bilayer film were calculated from the intersection of the two fits (18.2 mW cm^{-2} for RubDBP and 192 mW cm^{-2} for 1-CBPEA). Reproduced from ref. 60 with permission from the Royal Society of Chemistry, copyright 2022.

OSCs can be observed under direct excitation under 400 nm (Fig. 4c and d). A smaller driving force for charge extraction is expected for 1-CBPEA due to the higher triplet energy T_1, which results in a lower rate of charge extraction as detected by PL spectroscopy as well as a lower expected yield of triplet states. Accordingly, within the perovskite bilayer films, a stronger ESA is found for the rubrene $T_1 \rightarrow T_n$ transition than for 1-CBPEA at the ultrafast timescales investigated, respectively.

Once the spin-triplet states have been formed in the OSC, diffusion of the triplet states facilitate TTA-UC which can be tracked by time-resolved PL spectroscopy. The upconverted PL dynamics show two distinct features: (1) a rise time and (2) a decay. The rise feature is the convolution of the characteristic time of triplet generation, triplet diffusion, and TTA. As both triplet generation and TTA have been previously established on ultrafast time scales,[8] the triplet diffusion acts as the rate limiting step. The upconverted PL decay is rate-limited by the native triplet decay rate in solid state. We have previously shown that in the case of the annihilator rubrene, two distinct rise times can be found (Fig. 5a, top), and that the relative ratio of the two rise times is dependent on the triplet population.[7] A lower triplet population allows for the long-lived triplets to diffuse much further from the interface prior to TTA-UC (diffusion-mediated UC), while a high triplet population results in rapid TTA-UC close to the interface (interface-mediated UC). Due to the proximity to the perovskite, the singlets formed during interface-mediated UC are rapidly transferred back to the perovskite, reducing the apparent QY of this process. In comparison, for 1-CBPEA, a single rise time is observed (Fig. 5a, bottom), which can likely be attributed to the significantly shorter triplet lifetime ($\tau_{1\text{-CBPEA}}$ = 1 μs *vs.* τ_{Rub} > 10 μs).[60] Hence, all TTA-UC observed is expected to occur in a shorter time frame close to the interface.

The TTA-UC efficiency is uniquely dependent on the incident power and can be characterized by the intensity threshold I_{th}.[65] In a double-logarithmic plot of the UC PL intensity *vs.* incident power, the I_{th} is found as the intersect of a slope $\alpha = 2$ and $\alpha = 1$, due to the quadratic dependence of the UC PL on the incident power (I_{inc}) below I_{th}: $I_{UC} \propto I_{inc}$,[2] and the linear relationship above I_{th}: $I_{UC} \propto I_{inc}$. Above the threshold intensity, the generated triplets predominately decay through TTA-UC, and this is the regime where the UC process becomes efficient.[55] Mathematically first introduced by Monguzzi *et al.*,[65] the I_{th} can be described as:

$$I_{th} = \frac{\left(k_A^T\right)^2}{\phi_{tr}\alpha(E)\gamma_{TT}} \quad (3)$$

Here, k_A^T is the triplet decay rate, ϕ_{tr} the QY of triplet generation, $\alpha(E)$ is the absorption coefficient of the sensitizer, and

γ_{TT} the second-order rate constant characterizing the TTA process, a value unique to each annihilator.

Comparing the power dependence of the two annihilators reported to date in perovskite-sensitized UC, intensity thresholds of I_{th} = 18 mW cm^{-2} can be extracted for RubDBP and I_{th} = 195 mW cm^{-2} for 1-CBPEA (Fig. 5b).[60] As mentioned previously, the triplet lifetime of rubrene is an order of magnitude larger than that of 1-CBPEA. To first approximation, this would indicate an intensity threshold that is two orders of magnitude lower for the RubDBP system than for 1-CBPEA. However, since this is not experimentally verified, differences in γ_{TT} are required to account for the single order of magnitude difference. As stipulated by Monguzzi *et al.*, γ_{TT} is related to the probability of TTA-UC successfully generating a singlet state, the triplet exciton diffusion length, and the exciton interaction distance. Hence, γ_{TT} must be larger for 1-CBPEA than rubrene, indicating that the triplet diffusion rate or probability of TTA-UC must be higher.

Electronic effects and ion migration

In contrast to the other aforementioned triplet generation mechanisms where the triplet states are populated by energy transfer of localized excitons in the sensitizer, the fact that perovskite-sensitized UC is based on a highly defect-tolerant sensitizer and depends on the charge transfer at the interface between a bulk (generally) n-type perovskite and p-type OSC (rubrene) adds additional difficulty in fully characterizing the system.

Due to the differences in Fermi energies, a space charge region is generated at the interface of the perovskite and the OSC. Interfacing the predominately n-type perovskite with the p-type rubrene results in the perovskite bands bending upwards due to the perovskite acting as the donor space charge layers while the rubrene bands bend down. Effectively, this results in holes accumulating in rubrene, or 'precharging'.[87] This precharging effect allows for rapid triplet exciton formation upon initial illumination, causing an early time spike in the UC PL (Fig. 6a), which diminishes over the course of several seconds.[87–89]

Perovskites, while fully ionic materials, are considered 'soft' materials as ions can easily migrate in the perovskite upon the addition of a stressor such as light or an electric field.[90–95] This fact in concert with the high defect tolerance of perovskites[96] makes for interesting photophysical properties which can change over time. Upon illumination, ions migrate throughout the perovskite thin film and consequently can fill defect states or continue migrating through the film with the generated charges.[97–99] Additionally, defect states can be filled by charge carrier trapping, hence, the effect of illumination on the underlying perovskite sensitizer cannot be neglected. We have shown that the inherent trap density of the perovskite thin film is crucial in the UC yield.[37] However, changes in the trap density upon continued illumination have also proven to be important.[89] Under continuous illumination, both surface and bulk carrier trap states can be filled by the photoexcited free carriers, which has been shown to influence the perovskite

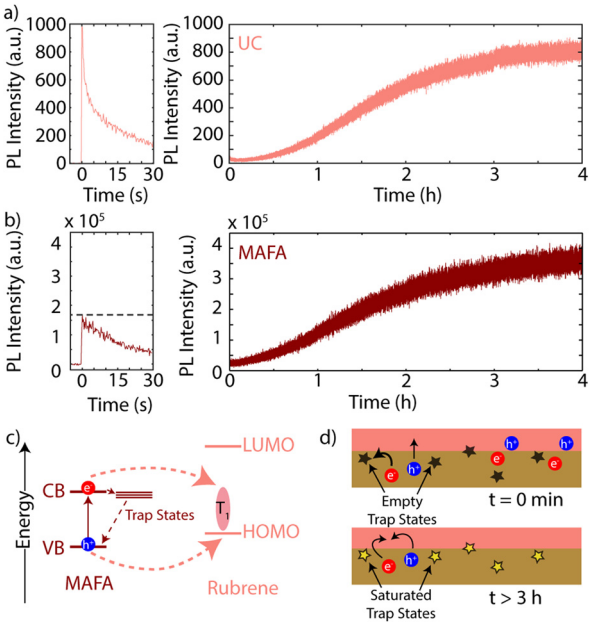

Fig. 6 (a) Intensity traces for the upconverted PL for MAFA/rubrene bilayer films for the first 30 s (left) and four hours (right) under constant illumination. (b) Intensity traces for MAFA only for the first 30 s (left) and four hours (right) under constant illumination. Data was collected under 780 nm puled excitation at a repetition frequency of 31.25 kHz and fluence of 32.4 mW cm^{-2}. (c) Energy graphic of triplet sensitization process for MAFA and rubrene highlighting the competing pathway way caused by trap states. (d) Illustration depicting the trap state filling occurring at the early times and saturation at later times allowing for efficient charge transfer. Adapted from ref. 89 with permission of AIP Publishing, copyright 2021.

PL QY where both photodarkening and photobrightening effects are possible. Under (solar-relevant) low fluences, we have observed initial photodarkening followed by a photobrightening of the underlying perovskite PL due to trap filling and ion migration (Fig. 6b), which coincides with an elongation of the perovskite PL lifetime over the course of four hours.[89] Concurrently, the UC PL photobrightens over the same time period (Fig. 6a), indicating that trap filling and charge transfer to the rubrene triplet state are competing processes (Fig. 6c and d).

Compositional tuning

One of the main benefits of perovskite semiconductors is their facile compositional tunability. The ABX_3 perovskite structure, where A is a monovalent cation, B a divalent cation and X an anion, allows for simple replacements of the A, B or X-site ions if the Goldschmidt tolerance factor t is maintained between $0.8 < t < 1$:

$$t = \frac{r_A + r_X}{\sqrt{2}(r_B + r_X)} \quad (4)$$

where r_A and r_B are the radii of the A and B-site cations and r_X is the anion radius, respectively.[100–102] Considering lead-based perovskite structures, common A-site cations include cesium

(Cs^+), methylammonium (MA^+) and formamidinium (FA^+), which are to date the most investigated cations. Structural distortions occur if the tolerance factor nears its limits, which can result in the formation of non-photoactive phases.[100] A prime example for the formation of non-photoactive phases is the affinity for FAMA to form the undesired δ-phase (yellow phase)[103] in contrast to the related MAFA composition due to the larger FA^+ cation than MA^+.

In addition to slight changes in the crystal structure, changing the A-site cation will have slight effects on the bandgap energy:[104–108] *e.g.*, MAFA has a bandgap of 1.59 eV while FAMA has a bandgap of 1.55 eV. Beyond simply changing the absolute bandgap, tuning the A-site cation has an influence on the absolute energy levels of the perovskite VB and CB. Olthof and co-workers have carefully investigated the absolute energy levels of a wide variety of perovskites and have shown that $FAPbI_3$ has a deeper VB at −6.24 eV and smaller bandgap (1.5 eV) than $MAPbI_3$, where the VB is at −5.93 eV with a bandgap of 1.6 eV.[109] Hence, the VB for FAMA is expected to be deeper than for MAFA, increasing the energetic driving force for hole transfer, albeit at the cost of the driving force for electron transfer.

The increase in driving force can be directly observed in the increased rate of quenching in the perovskite PL when FAMA (denoted as FO, FAMA overstoichiometric, indicating excess PbI_2 in the precursor stoichiometry) is interfaced with rubrene in contrast to overstoichiometric MAFA (denoted as O) (Fig. 7a–d). Concurrently with the increase in quenching for the formamidinium-rich perovskite sensitizer (FO), we find a higher UC PL intensity (Fig. 7e) indicating a higher yield of triplet formation in comparison to the overstoichiometric MAFA (O) and stoichiometric MAFA (S).

Changes in the X-site anion on the other hand have a much larger impact on the optical bandgap as well as band energy levels.[99,110–113] The addition bromide both deepens in the VB and moves the CB to a shallower level, resulting in a larger bandgap. Even a small addition of 15% results in an emission blueshift from 800 nm to 760 nm (Fig. 8a).[114] However, due to the facile ion movement in perovskite thin films, the addition of bromide causes additional difficulties: halide migration results in a rapid redshift of the PL under continued illumination at 400 nm (Fig. 8b), yielding local inhomogeneities of the optoelectronic properties.[98,112,115,116]

With increasing bromide content, the PL QY of the perovskite thin film increases, as does the PL lifetime due to an improvement in the crystallinity and a reduction in trap density.[114,117,118] Once interfaced with rubrene, quenching of the PL decay indicates efficient charge carrier extraction and emission is detected from RubDBP for all compositions under 780 nm excitation (Fig. 8c). The highest (external) UC PL intensity is observed for 5% bromide, while additional increase of the bromide content reduces the observed UC PL intensity (Fig. 8c, top). However, the change in the perovskite bandgap cannot be ignored, as it influences the amount of 780 nm light absorbed, and hence, the number of charge carriers generated in the perovskite sensitizer. Once normalized by the absorbance overlap with the 780 nm excitation laser, the 'internal' UC PL intensity increases with increasing bromide content (Fig. 8c, bottom), indicating that the change in the band alignment with increasing bromide content results in more favorable charge extraction. However, this observation also raises an interesting point: the perovskite is excited at 780 nm (1.59 eV) while the perovskite bandgap is shifted from 800 nm (1.55 eV) to 760 nm (1.69 eV). Hence, in the case of the highest bromide content, the bandgap is not excited directly. Rather, shallow traps are optically excited in the Urbach tail[119–121] and the generated carriers require ambient thermal energy to populate the band edge. Once the VB and CB are populated, charge extraction results in the generation of the rubrene triplet state T_1 (Fig. 8d).[114]

Therefore, two of the most critical aspects of efficient triplet generation at the perovskite/OSC interface can be traced back

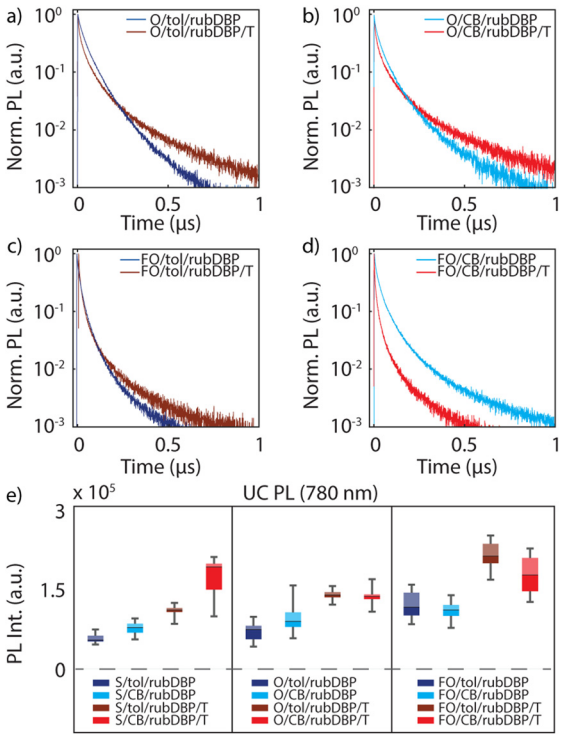

Fig. 7 Normalized perovskite PL decays for methylammonium-rich (a and b) and formamidinium-rich (c and d) perovskite bilayer films. Red curves/plots signify films treated with a post-fabrication thermal annealing step while blue traces/plots are unheated bilayer films. Darker shades correspond to RubDBP deposited from toluene (tol) while lighter shades correspond to RubDBP deposited from chlorobenzene (CB). All PL decays were taken under 780 nm pulsed excitation at a repetition frequency of 31.25 kHz at a power density of 4.84 mW cm^{-2}. (e) Box plots of the integrated upconverted PL emission across 30 spots for the perovskite bilayer films of varying treatments under 780 nm continuous wave excitation at a power density of 45.2 mW cm^{-2}. Comparison of the stoichiometric (S) and over-stoichiometric (O) addition of PbI_2 for the methylammonium-rich perovskite are shown in the left and center box plots, respectively. Formamidinium-rich perovskite box plots are shown on the right. Adapted from ref. 133 with permission of AIP Publishing, copyright 2020.

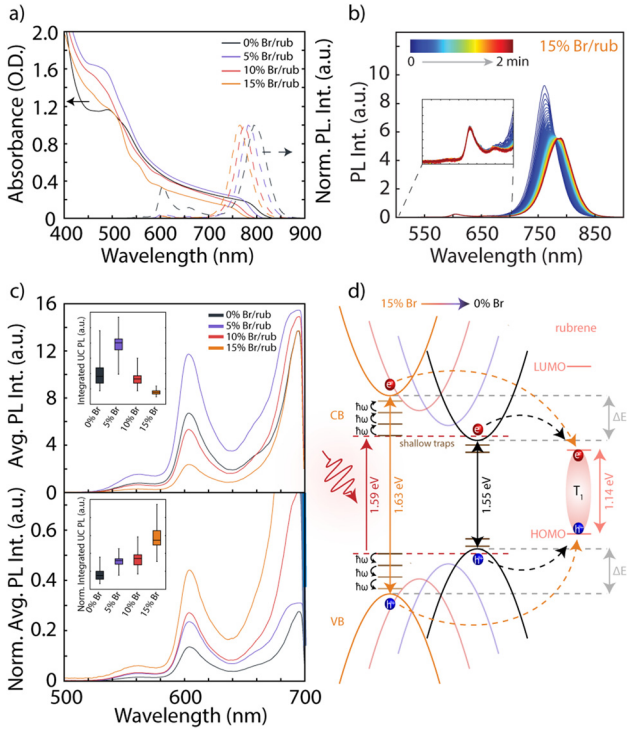

Fig. 8 (a) Absorption and normalized emission for $MA_{0.85}FA_{0.15}Pb(Br_xI_{1-x})$ perovskite bilayer films of varying bromide concentrations (x = 0, 5, 10, and 15). (b) Time-dependent PL measurement of the 15% bromide composition bilayer film where an observable bathochromic shift to the perovskite emission is observed. Inset magnifies the rubrene emission at 600 nm. All PL measurements were taken under 405 nm continuous wave excitation. (c) Average upconverted PL emission for the mixed halide MAFA bilayer films (top). Average upconverted PL emission of the mixed halide MAFA bilayer films normalized to the overlap integral of the film absorbance and 780 nm laser emission (bottom). Box plot insets in (c) show integrated upconverted PL intensities for the bilayer films taken across 20 spots for two sample sets. (d) Schematic illustrating the sensitization process assisted by trap-states within the perovskite for the mixed halide compositions. Adapted from ref. 114 with permission of AIP Publishing, copyright 2021.

to the carrier lifetime as well as the energetic driving force for both hole and electron extraction. In addition, a smaller bandgap is beneficial as this enables a higher absorbance at the desired low energy wavelengths. This emphasizes that a careful balance must be struck between absorption at the desired near-infrared wavelengths and charge extraction efficiency.

Fabrication methods and surface treatments

Due to the 'soft' ionic nature of perovskites and their strong susceptibility to their environment,[122–130] the fabrication conditions[89,131–133] and post-fabrication treatments[134–140] can be utilized to influence the device performance. To date, most perovskite-sensitized bilayer devices have been fabricated by two-step solution-based methods, where RubDBP is deposited onto the underlying perovskite film from either toluene (TOL) or chlorobenzene (CB), known antisolvents for perovskite synthesis to avoid dissolution of the underlying perovskite thin film.[36,37,133] To circumvent this second solution-based step during device fabrication, the annihilator can also be introduced in a 'one-step' method, where rubrene and DBP are added directly to the antisolvent during perovskite fabrication.[141] In addition to simplifying the fabrication method, this one-step approach can increase the surface area of the perovskite/OSC interface due to intercalation of rubrene molecules between grains, allowing for a greater extraction of charges.[141]

However, despite using known antisolvents for perovskite fabrication, we have observed that the different solvents, TOL and CB, used for RubDBP deposition yield different UC emission intensity based on the underlying perovskite composition (Fig. 7c).[133] This indicates that different solvents interact with the perovskite in a different manner. Similar to our approach of using different antisolvents for the rubrene deposition, MacQueen and co-workers have investigated the effect of the antisolvent used in the perovskite synthesis while using a constant solvent (CB) for the rubrene deposition. We have also investigated the influence of a post-fabrication solvent-treatment step on the UC performance, based on previous work by Baldo, Bawendi and co-workers. Of importance here is that to date, these three different groups that have reported on perovskite-sensitized UC have utilized three different perovskite compositions, as well as various perovskite fabrication methods and rubrene deposition methods. Hence, care must be taken when directly comparing the reported results as varying solvents will impact individual perovskite compositions differently. In the following, we will discuss the influence of the perovskite fabrication conditions and post-fabrication surface treatments in detail and discuss the role of the interfacial properties on the charge extraction.

In the seminal report of perovskite-sensitized UC,[36] a 14 nm thin FAMA perovskite film was utilized to obtain a similar optical density as previous solid-state PbS nanocrystal-based UC devices.[13,142] In particular, this approach was taken to minimize the effect of singlet back transfer or reabsorption of the upconverted photons, detrimental process in previous solid-state devices.[31] However, in perovskite-sensitized UC, reabsorption did not appear to be as much of a hinderance. By investigating the effect of the MAFA perovskite-film thickness,[37] we have been able to establish that the perovskite film thickness, crystal grain size and quality are key factors that influence the UC properties. With increasing film thickness, an increase in the average grain size is found, and a concurrent increase in the carrier lifetime due to a reduction in trap states. Furthermore, the effect of the perovskite film thickness is observed in the intensity threshold I_{th}. Since the absorption coefficient $\alpha(E)$ of the sensitizer is found in the denominator (*vide supra*), it is not surprising that the I_{th} is reduced with increasing thickness, resulting in sub-solar intensity threshold at the optimal perovskite film thickness of ~100 nm.[37]

To investigate the effect of the utilized antisolvent on the UC process, MacQueen and co-workers compared the UC performance of bilayer UC devices composed of ~500 nm thick $MAPbI_3$ films fabricated using either CB or anisole (ANI) as the

antisolvent with CB as the solvent for RubDBP.[88] By varying both the antisolvent as well as the antisolvent drip time, the authors inferred that a pinhole-free perovskite film of high quality yielding uniform and bright perovskite PL was a cornerstone of a high UC yield. However, this was not the only relevant factor. Both antisolvents investigated delivered similar $MAPbI_3$ PL intensities and underlying perovskite crystallite size and film structure, yet the ANI-based UC device outperformed the CB-based UC device by an order of magnitude. This is a clear indication that a more intricate mechanism is limiting the UC performance. Despite similar bulk performance, the authors found a significant difference in the perovskite carrier lifetimes as extracted by time-resolved PL, which is concurrent with difference in the UC PL intensity. A higher surface-defect density results in a shorter lifetime for the CB-based perovskite, which translates in less charges transferring to rubrene within their lifetime, and thus, a lower UC QY.[88] These results are a clear indication that the interfacial properties, carrier lifetimes and defect density are critical factors in the charge extraction process at the interface.

In addition to the changes in the perovskite fabrication methods, post-fabrication treatments can also be utilized to modify the perovskite surface properties. An example of such an investigation was performed by Wang *et al.*[143] where the authors studied the effect of post-fabrication solvent treatment on the UC properties. We highlight here, that in contrast to all previously discussed studies, here, rubrene and DBP were deposited by vapor deposition, decoupling the effect of the rubrene deposition and the solvent treatment. The study shows that the perovskite film treated with isopropanol (IPA) increases the UC PL QY, while TOL treatment results in a reduction of the UC PL QY, which agrees with the increased perovskite PL quenching observed for the IPA-treated UC device. The authors suggested that the polar solvent IPA can remove the precursors FAI and MAI,[143] generating surface traps while the nonpolar toluene reduces the number of surface traps and residual solvent. Therefore, the authors concluded that the observed surface traps are extending the carrier lifetime at the perovskite/OSC interface, and thus, mediating the triplet generation.

Expanding on this approach, we have recently investigated in detail the effect of seven different solvents on the perovskite-sensitized UC mechanism:[144] acetonitrile (ACN), ethanol (EtOH), IPA, 1-butanol (ButOH), TOL, CB and ANI. Following Taylor *et al.*,[145] the solvents can be classified into three categories. Type I solvents (IPA, EtOH, ButOH) readily dissolve the precursors MAI and FAI. Type II solvents (ANI, CB) show a higher solubility for FAI than MAI, and type III solvents (TOL) which readily decompose FAI and MAI resulting in I_2 and I_3^- which can be observed spectroscopically.[146,147] While ACN can be classified as type I, it is considered its own category as it fully dissolves MAFA perovskites and partially dissolves the FAMA composition.[144] Based on this solvent classification, the previous report of differing effects in the UC PL intensity when depositing rubrene from CB and TOL can simply be traced back to different effects of the solvent on the perovskite surface.[133]

In agreement with Wang *et al.*,[143] we found increased quenching of the perovskite PL in the presence of rubrene for ACN and type I solvents, while a reduction in the perovskite PL quenching is found for type II and type II solvents. However, single charge transfer, *i.e.*, hole transfer, is also expected to have this effect on the perovskite PL dynamics. To correlate the PL quenching to the triplet formation, TA spectroscopy was utilized, which shows an increased $T_1 \rightarrow T_n$ PIA for type I solvents over the control (untreated) and type II and type III solvents. The ACN film is slightly thinner due to the slight perovskite dissolution, hence the reduced $T_1 \rightarrow T_n$ PIA can be (in part) traced to a lower absorbance of the excitation laser.[144]

As expected, a higher UC PL intensity is observed in the case of a higher yield of triplet generation (Fig. 9a): ACN and type I antisolvents increase the UC PL intensity in comparison to the control, while type II and type III antisolvents reduce the UC PL intensity. The surface morphology for the control as measured by scanning tunneling microscopy (STM) is shown in the inset, and no changes are observed with solvent treatment, indicating that the underlying topographical structure is not affected.[144]

Detailed structural investigation by X-ray diffraction indicate that polar solvents reduce the intensity of the reflection related to the undesired δ-phase (yellow phase) and slight growth of PbI_2 is found.[103] In contrast to previous reports, we do find that treatment with TOL forms PbI_2, likely due to iodine expulsion after FAI/MAI decomposition, particularly upon extended soaking of the perovskite film.[148,149]

Clearly, even though these solvents have been classified as antisolvents for perovskite synthesis, the perovskite properties and composition are influenced, and the perovskite film cannot be considered as inert to the influence of the solvents. Considering that each solvent type is expected to uniquely influence certain parts of the perovskite crystal structure, a change in the electronic structure as the underlying cause of the change in the UC QY would not be surprising. However, no changes in the crystal structure are observed upon the short contact period during spin coating, indicating that the RubDBP deposition is not expected to have a drastic effect on the underlying perovskite quality.[103]

Scanning tunneling spectroscopy (STS) is uniquely qualified to give insight into the surface properties of the perovskite thin film, as well as the relative position of the VB and CB with respect to the Fermi level E_F, defined at 0 V. Here, the STM tip is parked above the surface and the tunneling current is recorded as a function of the applied bias. If E_F is found close to the VB, the perovskite surface is p-type, while E_F close to the CB indicates an n-type termination.[150] In the case of an intrinsic semiconductor E_F is centered between the VB and CB. As shown in Fig. 9c, a shift toward a more n-type perovskite is observed for the FAMA treated with polar solvents (type I and ACN), while on the other hand, type II and type III solvents shift the surface doping to a p-type semiconductor.

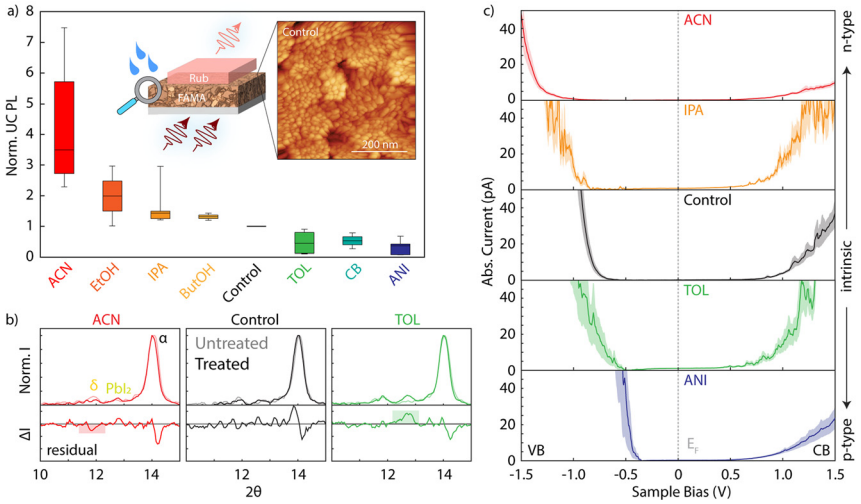

Fig. 9 (a) Box plots of upconverted PL intensities under 780 nm excitation. The spectra were integrated from 500 nm to 610 nm across numerous spots for the solvent treated FAMA/Rub bilayer films and normalized to the UC PL intensity of the untreated FAMA/Rub control for comparison. The inset shows the device structure and a scanning tunneling microscopy topography of the FAMA control film taken at −0.8 V and −100 pA. (b) Grazing incidence X-ray diffraction for the acetonitrile (ACN), control, and toluene (TOL) treated perovskite only films pre- (lighter shade) and post-solvent treatment (darker shade). Patterns were normalized to the perovskite (110) peak at 14° to aid comparison. The residuals highlight the change after the solvent treatment. (c) Average scanning tunneling spectroscopy (STS) *IV* curves for the solvent treated perovskite only films. Shaded regions depict the 95% confidence interval for each sample set. All curves were measured from −2.0 to 2.0 V at a rate of 1.0 V s^{-1}. The tip was set to a bias of −1.5 V and setpoint current of −100 pA and stabilized between each IV spectra. Adapted with permission from ref. 144. Copyright 2022 John Wiley and Sons.

Hence, the effect of solvent treatment can be traced back to changes in the built-in potential of the perovskite/OSC interface and band bending behavior. Band bending is one of the unique differences of this triplet sensitization mechanism over other systems.[151–154] Rubrene is an inherently p-type semiconductor, and the interfacial band bending will be influenced strongly by the Fermi level of the perovskite. In the case of an n-type perovskite, the Fermi level of the perovskite can be higher than that of rubrene, and the perovskite becomes the donor space charge layer resulting in upward band bending of the perovskite, shown in Fig. 10. This causes hole accumulation at the surface and an increase in driving force for electron extraction. However, electrons will migrate into the bulk of the perovskite over time, limiting the number of triplets generated. On the other hand, a p-type perovskite has a lower Fermi level than rubrene, which results in downward band bending of the perovskite and upward band bending of rubrene, which results in hole migration away from the interface. However, as hole transfer is the first prerequisite step of triplet formation, this minimizes the achievable triplet QY.

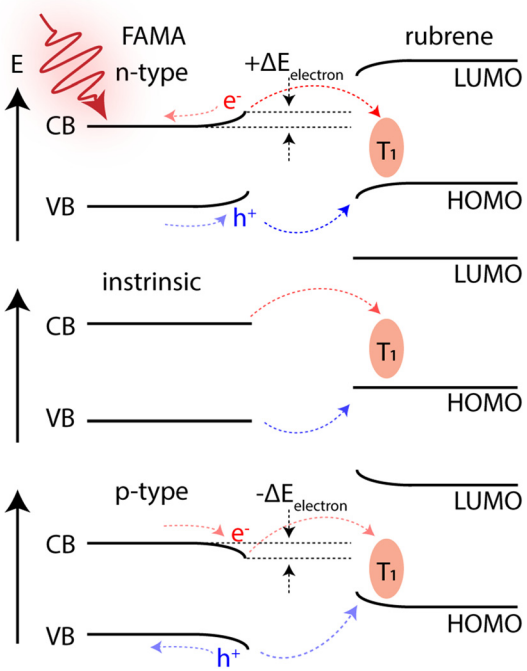

Fig. 10 Schematic illustrating band bending at the perovskite/rubrene interface showing the difference from n-type, intrinsic, and p-type doping of FAMA. Upward band bending of the n-type FAMA allows hole accumulation at the surface while downwards band bending in p-type semiconductors pushes holes away from the interface. Adapted with permission from ref. 144. Copyright 2022 John Wiley and Sons.

Effects of triplet charge annihilation

One of the largest controversies of perovskite-sensitized UC is the role of triplet-charge annihilation (TCA). It is not unexpected that TCA may be a key factor in reducing the obtained UC QY, as rubrene is a known hole transport layer for perovskite solar cells and triplet formation at the interface is not a unity process. However, to date, the role of TCA in the UC process is still unclear. Due to the negative magnetic field

effect (MFE) on the UC PL off TTA-UC and positive MFE of TCA,[155–158] magneto-PL studies[159–161] are a common approach to investigate whether TCA is competing with TTA. Wang *et al.*[143] reported a smaller MFE for IPA-treated UC devices than for the TOL-treated counterparts, which was attributed to stronger TCA. In agreement with this result, we have found that at high incident power densities, the MFE of type II and type III shows a higher magnitude than the type I and ACN counterparts.[144] However, at incident power densities on the order of 1 sun (100 mW cm^{-2}),[162] the magnitude of the MFE is slightly higher for ACN and type I antisolvents than for the type II and type III solvents and the overall MFE is much larger than at high power densities. Hence, we urge caution in the interpretation of these results, as the magnitude of the MFE is strongly dependent on the triplet population.[142,163] It is established that the triplet population for type II and type III solvents is lower than for the type I solvents (*vide supra*), hence, a larger MFE is expected. Additional studies will be required to fully unravel the role of TCA on the TTA-UC process in these devices.

Intermolecular interactions

Thus far, we have discussed in detail the influence of the perovskite properties. However, the OSC properties cannot be neglected either. Particularly in the case of the two successful annihilators reported to date, RubDBP and 1-CBPEA, both capable of SF and TTA-UC, the molecular interactions are key aspects that cannot be ignored. Vapor-deposited polycrystalline rubrene films have shown a 19-fold increase in the UC PL intensity upon DBP doping,[13] which can be attributed to the harvesting of the excited state prior to the triplet pair separation step of SF.[6] On the other hand, we have observed very little influence in the UC PL intensity for amorphous solution-fabricated RubDBP thin films.[164] This can be traced back to the local environment of the rubrene molecules. While a crystalline, close packing of the OSC is required for SF to occur efficiently, more disorder is allowed in the case of TTA-UC.[165,166] Hence, disorder can be utilized to tune the rates of the forward TTA-UC and reverse SF process.

Similarly, work by Wasielewski and co-workers has indicated that in the 1-CBPEA parent molecule (9,10-bisphenyl ethynyl)anthracene (BPEA), the fabrication method directly impacts the OSC PL QY due to changes in the SF rates.[167,168] Due to the similarity of BPEA and 1-CBPEA, an analogous effect is expected here, and additional work will be required to optimize the OSC layer.

Therefore, OSC engineering by means of the deposition solvent,[164] post-fabrication heat treatments to drive off excess solvent and induce some long-range crystallinity[133] and a careful control of solvent evaporation rates may be the key to improving the overall device performance.

Outlook

In the last few years, strides have been made in understanding the fundamental requirements for triplet sensitization at the perovskite/OSC interface. Most of the work has focused on the underlying perovskite properties and the perovskite/rubrene interface. However, rubrene is clearly not the annihilator of choice for practical applications of perovskite-sensitized TTA-UC due to the inherent energy mismatch. Additional annihilators must be investigated, with a particular focus on annihilators with a triplet energy of $\sim E(T_1)$ = 1.5 eV, with well-matched energy levels. Of particular interest are additional tetracene and perylene derivatives, as well as promising additional anthracene derivatives. The successful application of 1-CBPEA in perovskite-sensitized UC emphasizes the promise of additional closely related anthracene derivatives such as 2-methyl-9,10-bis(naphthalene-2-yl)anthracene[169] or BPEA.[167]

However, care must be taken to not screen the potential candidates for novel annihilators based on their solution-phase properties, rather the effects of intermolecular coupling must be considered in solid state. These intermolecular interactions can lead to a variety of effects that greatly change the underlying exciton dynamics, shown in Fig. 11. Intermolecular coupling can induce (i) SF,[170] (ii) enable TTA,[10] (iii) result in delocalized excimer or exciplex states,[171] (iv) and even lead to aggregation-induced effects such as H- and J-type aggregation.[172] J-aggregation results in a small bathochromic shift of the absorption and emission as well as a strong increase in the absorption cross-section and the emission intensity. H-aggregation results in a hypsochromic shift of the absorption and quenching of the fluorescence, highlighted in Fig. 11.[173]

Intermolecular coupling effects can already be observed in the two annihilators (rubrene and 1-CBPEA) discussed here. In the solid state, intermolecular interactions enable both SF and TTA,[60] and 1-CBPEA exhibits a significantly redshifted absorption feature caused by aggregation, and significantly redshifted emission. Considering that Schmidt and co-workers have demonstrated that excimer formation can be used to reduce

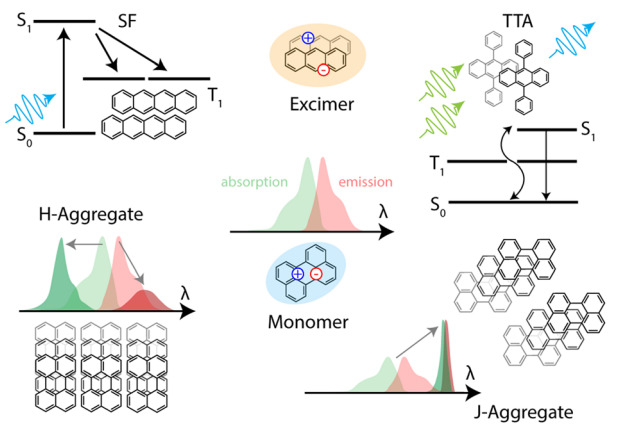

Fig. 11 Overview of the possible excitonic interactions occurring in OSC thin films: SF, TTA, excimer formation, and H- and J-aggregation. The cartoon of the difference in absorption (green) and emission (red) spectra are shown for the H- and J-aggregates (line) in comparison to the monomer (shaded).

the effects of SF,[70] and fabrication methods can tailor crystal arrangements as shown by Wasielewski and co-workers, which directly influence the intermolecular coupling in bis(phenylethynyl)anthracene (BPEA) and result in a change in the rate of SF,[167] these observations indicate that intermolecular couplings can be utilized to engineer the singlet and triplet energy surfaces to facilitate TTA-UC while suppressing unwanted relaxation pathways.

Aggregation-induced effects may also be able to lower the singlet energy level S_1 with respect to the triplet energy T_1, validating the requirement for TTA-UC: $E(S_1) = 2E(T_1)$ and enabling TTA-UC to occur. Hence a clear understanding of the OSC properties in solid state will form the foundation for future advancements in solid-state UC.

In addition to the OSC layer, a key limitation of current perovskite-sensitized TTA-UC devices is the low efficiency of charge extraction as indicated by the strong residual perovskite PL of the bilayer devices, resulting in a low triplet QY and thus, low Φ_{UC}.[142,143] While in a conventional photovoltaic, the built-in potential pulls individual charges to the respective electrodes at which they are extracted, here, we are extracting both charges at the same interface. Therefore, there is little driving force for both charges to migrate to the interface. Utilizing band bending and further built-in potential tuning may provide an avenue to increase charge extraction.

Conclusion

In conclusion, triplet generation at the perovskite/OSC interface is a universal phenomenon if the fundamental energy levels of the bulk lead halide perovskite sensitizer and annihilator are well matched. Despite significant progress in understanding the complex underlying photophysical processes occurring, the field of perovskite-sensitized UC is still in its infancy and is rapidly expanding. To continue to advance the field, future work should be focused on identifying additional annihilators to expand the library of viable perovskite/annihilator pairs and increasing the efficiency of charge extraction and triplet formation. In addition to investigating the properties of the perovskite/OSC bilayers, unraveling the complex processes occurring in solid-state OSC thin films will pave the way toward more efficient UC devices with a larger apparent anti-Stokes shift.

Conflicts of interest

FSU has filed a provisional application for a U.S. patent based on this technology that names L.N. as an inventor.

Acknowledgements

The authors acknowledge funding by Florida State University.

References

1 G. C. Smith, *Phys. Rev.*, 1968, **166**, 839–847.
2 J. B. Metternich and R. Gilmour, *J. Am. Chem. Soc.*, 2015, **137**, 11254–11257.
3 K. Singh, S. J. Staig and J. D. Weaver, *J. Am. Chem. Soc.*, 2014, **136**, 5275–5278.
4 M. Teders, C. Henkel, L. Anhäuser, F. Strieth-Kalthoff, A. Gómez-Suárez, R. Kleinmans, A. Kahnt, A. Rentmeister, D. Guldi and F. Glorius, *Nat. Chem.*, 2018, **10**, 981–988.
5 D. A. Nicewicz and D. W. C. MacMillan, *Science*, 2008, **322**, 77–80.
6 D. G. Bossanyi, Y. Sasaki, S. Wang, D. Chekulaev, N. Kimizuka, N. Yanai and J. Clark, *J. Mater. Chem. C*, 2022, **10**, 4684–4696.
7 S. Wieghold, A. S. Bieber, Z. A. VanOrman and L. Nienhaus, *J. Phys. Chem. Lett.*, 2019, **10**, 3806–3811.
8 C. R. Conti, A. S. Bieber, Z. A. VanOrman, G. Moller, S. Wieghold, R. D. Schaller, G. F. Strouse and L. Nienhaus, *ACS Energy Lett.*, 2022, 617–623.
9 D. L. Dexter, *J. Chem. Phys.*, 1953, **21**, 836–850.
10 T. N. Singh-Rachford and F. N. Castellano, *Coord. Chem. Rev.*, 2010, **254**, 2560–2573.
11 A. Monguzzi, R. Tubino and F. Meinardi, *J. Phys. Chem.*, 2009, **113**, 1171–1174.
12 S. Amemori, Y. Sasaki, N. Yanai and N. Kimizuka, *J. Am. Chem. Soc.*, 2016, **138**, 8702–8705.
13 M. Wu, D. N. Congreve, M. W. B. Wilson, J. Jean, N. Geva, M. Welborn, T. Van Voorhis, V. Bulović, M. G. Bawendi and M. A. Baldo, *Nat. Photonics*, 2016, **10**, 31–34.
14 Z. Huang, X. Li, B. D. Yip, J. M. Rubalcava, C. J. Bardeen and M. L. Tang, *Chem. Mater.*, 2015, **27**, 7503–7507.
15 K. Mase, K. Okumura, N. Yanai and N. Kimizuka, *Chem. Commun.*, 2017, **53**, 8261–8264.
16 M. Koharagi, N. Harada, K. Okumura, J. Miyano, S. Hisamitsu, N. Kimizuka and N. Yanai, *Nanoscale*, 2021, **13**, 19890–19893.
17 K. Okumura, N. Yanai and N. Kimizuka, *Chem. Lett.*, 2019, **48**, 1347–1350.
18 S. He, X. Luo, X. Liu, Y. Li and K. Wu, *J. Phys. Chem. Lett.*, 2019, **10**, 5036–5040.
19 P. Xia, E. K. Raulerson, D. Coleman, C. S. Gerke, L. Mangolini, M. L. Tang and S. T. Roberts, *Nat. Chem.*, 2020, **12**, 137–144.
20 X. Luo, Y. Han, Z. Chen, Y. Li, G. Liang, X. Liu, T. Ding, C. Nie, M. Wang, F. N. Castellano and K. Wu, *Nat. Commun.*, 2020, **11**, 28.
21 C. M. Papa, S. Garakyaraghi, D. B. Granger, J. E. Anthony and F. N. Castellano, *Chem. Sci.*, 2020, **11**, 5690–5696.
22 S. He, R. Lai, Q. Jiang, Y. Han, X. Luo, Y. Tian, X. Liu and K. Wu, *Angew. Chem., Int. Ed.*, 2020, **59**, 17726.
23 J. A. Bender, E. K. Raulerson, X. Li, T. Goldzak, P. Xia, T. Van Voorhis, M. L. Tang and S. T. Roberts, *J. Am. Chem. Soc.*, 2018, **140**, 7543–7553.
24 J. Alves, J. Feng, L. Nienhaus and T. W. Schmidt, *J. Mater. Chem. C*, 2022, **10**, 7783–7798.

25 Z. A. VanOrman, H. K. Drozdick, S. Wieghold and L. Nienhaus, *J. Mater. Chem. C*, 2021, **9**, 2685–2694.
26 A. J. Carrod, V. Gray and K. Börjesson, *Energy Environ. Sci.*, 2022, **15**, 4982–5016.
27 J. Zhou, Q. Liu, W. Feng, Y. Sun and F. Li, *Chem. Rev.*, 2015, **115**, 395–465.
28 B. S. Richards, D. Hudry, D. Busko, A. Turshatov and I. A. Howard, *Chem. Rev.*, 2021, **121**, 9165–9195.
29 V. Gray, K. Moth-Poulsen, B. Albinsson and M. Abrahamsson, *Coord. Chem. Rev.*, 2018, **362**, 54–71.
30 Z. A. VanOrman and L. Nienhaus, *ACS Energy Lett.*, 2021, **6**, 3686–3694.
31 N. Geva, L. Nienhaus, M. Wu, V. Bulović, M. A. Baldo, T. Van Voorhis and M. G. Bawendi, *J. Phys. Chem. Lett.*, 2019, **10**, 3147–3152.
32 S. D. Stranks, G. E. Eperon, G. Grancini, C. Menelaou, M. J. P. Alcocer, T. Leijtens, L. M. Herz, A. Petrozza and H. J. Snaith, *Science*, 2013, **342**, 341–344.
33 W. Tress, N. Marinova, O. Inganäs, M. K. Nazeeruddin, S. M. Zakeeruddin and M. Graetzel, *Adv. Energy Mater.*, 2015, **5**, 1400812.
34 G. Xing, N. Mathews, S. Sun, S. S. Lim, Y. M. Lam, M. Grätzel, S. Mhaisalkar and T. C. Sum, *Science*, 2013, **342**, 344–347.
35 M. M. Lee, J. Teuscher, T. Miyasaka, T. N. Murakami and H. J. Snaith, *Science*, 2012, **338**, 643–647.
36 L. Nienhaus, J.-P. Correa-Baena, S. Wieghold, M. Einzinger, T.-A. Lin, K. E. Shulenberger, N. D. Klein, M. Wu, V. Bulović, T. Buonassisi, M. A. Baldo and M. G. Bawendi, *ACS Energy Lett.*, 2019, 888–895.
37 S. Wieghold, A. S. Bieber, Z. A. VanOrman, L. Daley, M. Leger, J.-P. Correa-Baena and L. Nienhaus, *Matter*, 2019, **1**, 705–719.
38 R. R. Islangulov, D. V. Kozlov and F. N. Castellano, *Chem. Commun.*, 2005, 3776–3778.
39 R. R. Islangulov and F. N. Castellano, *Angew. Chem., Int. Ed.*, 2006, **45**, 5957–5959.
40 S. Baluschev, V. Yakutkin, T. Miteva, G. Wegner, T. Roberts, G. Nelles, A. Yasuda, S. Chernov, S. Aleshchenkov and A. Cheprakov, *New J. Phys.*, 2008, **10**, 013007.
41 P. B. Merkel and J. P. Dinnocenzo, *J. Lumin.*, 2009, **129**, 303–306.
42 Z. A. VanOrman, A. S. Bieber, S. Wieghold and L. Nienhaus, *Chem. Mater.*, 2020, **32**, 4734–4742.
43 Z. A. VanOrman, C. R. Conti, G. F. Strouse and L. Nienhaus, *Chem. Mater.*, 2021, **33**, 452–458.
44 C. J. Imperiale, P. B. Green, M. Hasham and M. W. B. Wilson, *Chem. Sci.*, 2021, **12**, 14111–14120.
45 R. Lai, Y. Sang, Y. Zhao and K. Wu, *J. Am. Chem. Soc.*, 2020, **142**, 19825–19829.
46 K. Mase, K. Okumura, N. Yanai and N. Kimizuka, *Chem. Commun.*, 2017, **53**, 8261–8264.
47 S. Wieghold, Z. A. VanOrman and L. Nienhaus, *Adv. Opt. Mater.*, 2021, **9**, 2001470.
48 N. Thantu, *J. Lumin.*, 2005, **111**, 17–24.
49 N. M. Lawandy and R. L. MacDonald, *J. Opt. Soc. Am. B*, 1991, **8**, 1307–1314.
50 E. V. Makeev and S. E. Skipetrov, *Opt. Commun.*, 2003, **224**, 139–147.
51 K. W. Krämer, D. Biner, G. Frei, H. U. Güdel, M. P. Hehlen and S. R. Lüthi, *Chem. Mater.*, 2004, **16**, 1244–1251.
52 S. Heer, K. Kömpe, H.-U. Güdel and M. Haase, *Adv. Mater.*, 2004, **16**, 2102–2105.
53 W. Wu, H. Guo, W. Wu, S. Ji and J. Zhao, *J. Org. Chem.*, 2011, **76**, 7056–7064.
54 M. Mahboub, H. Maghsoudiganjeh, A. M. Pham, Z. Huang and M. L. Tang, *Adv. Funct. Mater.*, 2016, **26**, 6091–6097.
55 Y. Y. Cheng, T. Khoury, R. G. C. R. Clady, M. J. Y. Tayebjee, N. J. Ekins-Daukes, M. J. Crossley and T. W. Schmidt, *Phys. Chem. Chem. Phys.*, 2010, **12**, 66–71.
56 R. Piper, M. Yoshida, N. Ekins-Daukes, S. Haque, Y. Y. Cheng, B. Fückel, T. Khoury, R. G. C. R. Clady, M. J. Y. Tayebjee, M. J. Crossley and T. W. Schmidt, in *2011 37th IEEE Photovoltaic Specialists Conference*, 2011, pp. 003632–003635.
57 Y. Y. Cheng, B. Fückel, T. Khoury, R. G. C. R. Clady, M. J. Y. Tayebjee, N. J. Ekins-Daukes, M. J. Crossley and T. W. Schmidt, *J. Phys. Chem. Lett.*, 2010, **1**, 1795–1799.
58 J.-H. Olivier, Y. Bai, H. Uh, H. Yoo, M. J. Therien and F. N. Castellano, *J. Phys. Chem. A*, 2015, **119**, 5642–5649.
59 T. F. Schulze, J. Czolk, Y.-Y. Cheng, B. Fückel, R. W. MacQueen, T. Khoury, M. J. Crossley, B. Stannowski, K. Lips, U. Lemmer, A. Colsmann and T. W. Schmidt, *J. Phys. Chem. C*, 2012, **116**, 22794–22801.
60 C. M. Sullivan and L. Nienhaus, *Nanoscale*, 2022, **14**, 17254–17261.
61 B. Manna, R. Ghosh and D. K. Palit, *J. Phys. Chem. C*, 2015, **119**, 10641–10652.
62 T. Fujino and T. Tahara, *J. Phys. Chem. B*, 2003, **107**, 5120–5122.
63 J. J. Burdett, A. M. Müller, D. Gosztola and C. J. Bardeen, *J. Chem. Phys.*, 2010, **133**, 144506.
64 T.-S. Ahn, A. M. Müller, R. O. Al-Kaysi, F. C. Spano, J. E. Norton, D. Beljonne, J.-L. Brédas and C. J. Bardeen, *J. Chem. Phys.*, 2008, **128**, 054505.
65 A. Monguzzi, J. Mezyk, F. Scotognella, R. Tubino and F. Meinardi, *Phys. Rev. B: Condens. Matter Mater. Phys.*, 2008, **78**, 195112.
66 T. Miyashita, P. Jaimes, T. Lian, M. L. Tang and Z. Xu, *J. Phys. Chem. Lett.*, 2022, **13**, 3002–3007.
67 E. M. Rigsby, T. Miyashita, P. Jaimes, D. A. Fishman and M. L. Tang, *J. Chem. Phys.*, 2020, **153**, 114702.
68 Z. Huang and M. L. Tang, *J. Phys. Chem. Lett.*, 2018, **9**, 6198–6206.
69 A. Nandi, B. Manna and R. Ghosh, *Phys. Chem. Chem. Phys.*, 2019, **21**, 11193–11202.
70 C. B. Dover, J. K. Gallaher, L. Frazer, P. C. Tapping, A. J. Petty, M. J. Crossley, J. E. Anthony, T. W. Kee and T. W. Schmidt, *Nat. Chem.*, 2018, **10**, 305–310.
71 S. Paul and V. Karunakaran, *J. Phys. Chem. B*, 2022, **126**, 1054–1062.

72 G. Ji, G. Zheng, B. Zhao, F. Song, X. Zhang, K. Shen, Y. Yang, Y. Xiong, X. Gao, L. Cao and D.-C. Qi, *Phys. Chem. Chem. Phys.*, 2017, **19**, 6546–6553.
73 M. M. Tavakoli, R. Tavakoli, D. Prochowicz, P. Yadav and M. Saliba, *Mol. Syst. Des. Eng.*, 2018, **3**, 717–722.
74 D. Wei, F. Ma, R. Wang, S. Dou, P. Cui, H. Huang, J. Ji, E. Jia, X. Jia, S. Sajid, A. M. Elseman, L. Chu, Y. Li, B. Jiang, J. Qiao, Y. Yuan and M. Li, *Adv. Mater.*, 2018, **30**, 1707583.
75 N. Droseros, B. Dänekamp, D. Tsokkou, P. P. Boix and N. Banerji, *APL Mater.*, 2019, **7**, 041115.
76 K. G. Stamplecoskie, J. S. Manser and P. V. Kamat, *Energy Environ. Sci.*, 2015, **8**, 208–215.
77 J. S. Manser and P. V. Kamat, *Nat. Photonics*, 2014, **8**, 737–743.
78 B. A. Chen, G. T. Pang, X. Q. Lan, Z. B. He and R. Chen, *Mater. Today Phys.*, 2020, **14**, 100228.
79 B. Anand, S. Sampat, E. O. Danilov, W. Peng, S. M. Rupich, Y. J. Chabal, Y. N. Gartstein and A. V. Malko, *Phys. Rev. B*, 2016, **93**, 161205.
80 M. Ullah, S. D. Yambem, E. G. Moore, E. B. Namdas and A. K. Pandey, *Adv. Electron. Mater.*, 2015, **1**, 1500229.
81 T. Wu, W. Ni, G. G. Gurzadyan and L. Sun, *RSC Adv.*, 2021, **11**, 4639–4645.
82 L. Ma, G. Galstyan, K. Zhang, C. Kloc, H. Sun, C. Soci, M. E. Michel-Beyerle and G. G. Gurzadyan, *J. Chem. Phys.*, 2013, **138**, 184508.
83 J. T. DuBose, G. Szabó, J. Chakkamalayath and P. V. Kamat, *J. Phys. Chem. A*, 2022, **126**, 7147–7158.
84 M. B. Price, J. Butkus, T. C. Jellicoe, A. Sadhanala, A. Briane, J. E. Halpert, K. Broch, J. M. Hodgkiss, R. H. Friend and F. Deschler, *Nat. Commun.*, 2015, **6**, 8420.
85 J. Fu, Q. Xu, G. Han, B. Wu, C. H. A. Huan, M. L. Leek and T. C. Sum, *Nat. Commun.*, 2017, **8**, 1300.
86 J. W. M. Lim, D. Giovanni, M. Righetto, M. Feng, S. G. Mhaisalkar, N. Mathews and T. C. Sum, *J. Phys. Chem. Lett.*, 2020, **11**, 2743–2750.
87 S. Wieghold and L. Nienhaus, *J. Phys. Chem. Lett.*, 2020, **11**, 601–607.
88 K. Prashanthan, B. Naydenov, K. Lips, E. Unger and R. W. MacQueen, *J. Chem. Phys.*, 2020, **153**, 164711.
89 Z. A. VanOrman, J. Lackner, S. Wieghold, K. Nienhaus, G. U. Nienhaus and L. Nienhaus, *Appl. Phys. Lett.*, 2021, **118**, 203903.
90 S. Wieghold, E. M. Cope, G. Moller, N. Shirato, B. Guzelturk, V. Rose and L. Nienhaus, *ACS Energy Lett.*, 2022, **7**, 2211–2218.
91 S. Bae, S. Kim, S.-W. Lee, K. J. Cho, S. Park, S. Lee, Y. Kang, H.-S. Lee and D. Kim, *J. Phys. Chem. Lett.*, 2016, **7**, 3091–3096.
92 T. Leijtens, E. T. Hoke, G. Grancini, D. J. Slotcavage, G. E. Eperon, J. M. Ball, M. De Bastiani, A. R. Bowring, N. Martino, K. Wojciechowski, M. D. McGehee, H. J. Snaith and A. Petrozza, *Adv. Energy Mater.*, 2015, **5**, 1500962.
93 D. Ji, M. Na, S. Wang, H. Zhang, K. Zhu, C. Zhang and X. Li, *Sci. Rep.*, 2018, **8**, 12492.
94 W. Tress, N. Marinova, T. Moehl, S. M. Zakeeruddin, M. K. Nazeeruddin and M. Grätzel, *Energy Environ. Sci.*, 2015, **8**, 995–1004.
95 T. Elmelund, B. Seger, M. Kuno and P. V. Kamat, *ACS Energy Lett.*, 2020, **5**, 56–63.
96 J. R. Poindexter, R. L. Z. Hoye, L. Nienhaus, R. C. Kurchin, A. E. Morishige, E. E. Looney, A. Osherov, J.-P. Correa-Baena, B. Lai, V. Bulović, V. Stevanović, M. G. Bawendi and T. Buonassisi, *ACS Nano*, 2017, **11**, 7101–7109.
97 Y. Yuan and J. Huang, *Acc. Chem. Res.*, 2016, **49**, 286–293.
98 M. C. Brennan, S. Draguta, P. V. Kamat and M. Kuno, *ACS Energy Lett.*, 2018, **3**, 204–213.
99 T. Elmelund, R. A. Scheidt, B. Seger and P. V. Kamat, *ACS Energy Lett.*, 2019, **4**, 1961–1969.
100 J.-P. Correa-Baena, M. Saliba, T. Buonassisi, M. Grätzel, A. Abate, W. Tress and A. Hagfeldt, *Science*, 2017, **358**, 739–744.
101 G. Grancini and M. K. Nazeeruddin, *Nat. Rev. Mater.*, 2019, **4**, 4–22.
102 Q. A. Akkerman, G. Rainò, M. V. Kovalenko and L. Manna, *Nat. Mater.*, 2018, **17**, 394–405.
103 F. Ma, J. Li, W. Li, N. Lin, L. Wang and J. Qiao, *Chem. Sci.*, 2017, **8**, 800–805.
104 N. Pellet, P. Gao, G. Gregori, T.-Y. Yang, M. K. Nazeeruddin, J. Maier and M. Grätzel, *Angew. Chem., Int. Ed.*, 2014, **53**, 3151–3157.
105 A. Amat, E. Mosconi, E. Ronca, C. Quarti, P. Umari, Md. K. Nazeeruddin, M. Grätzel and F. De Angelis, *Nano Lett.*, 2014, **14**, 3608–3616.
106 I. Borriello, G. Cantele and D. Ninno, *Phys. Rev. B: Condens. Matter Mater. Phys.*, 2008, **77**, 235214.
107 Y.-K. Jung, J.-H. Lee, A. Walsh and A. Soon, *Chem. Mater.*, 2017, **29**, 3181–3188.
108 C. C. Stoumpos, C. D. Malliakas and M. G. Kanatzidis, *Inorg. Chem.*, 2013, **52**, 9019–9038.
109 S. Tao, I. Schmidt, G. Brocks, J. Jiang, I. Tranca, K. Meerholz and S. Olthof, *Nat. Commun.*, 2019, **10**, 2560.
110 R. Lindblad, N. K. Jena, B. Philippe, J. Oscarsson, D. Bi, A. Lindblad, S. Mandal, B. Pal, D. D. Sarma, O. Karis, H. Siegbahn, E. M. J. Johansson, M. Odelius and H. Rensmo, *J. Phys. Chem. C*, 2015, **119**, 1818–1825.
111 I. M. Pavlovetc, A. Ruth, I. Gushchina, L. Ngo, S. Zhang, Z. Zhang and M. Kuno, *ACS Energy Lett.*, 2021, **6**, 2064–2071.
112 E. T. Hoke, D. J. Slotcavage, E. R. Dohner, A. R. Bowring, H. I. Karunadasa and M. D. McGehee, *Chem. Sci.*, 2015, **6**, 613–617.
113 S. Meloni, G. Palermo, N. Ashari-Astani, M. Grätzel and U. Rothlisberger, *J. Mater. Chem.*, 2016, **4**, 15997–16002.
114 A. S. Bieber, Z. A. VanOrman, H. K. Drozdick, R. Weiss, S. Wieghold and L. Nienhaus, *J. Chem. Phys.*, 2021, **155**, 234706.
115 B. Park, B. Philippe, S. M. Jain, X. Zhang, T. Edvinsson, H. Rensmo, B. Zietz and G. Boschloo, *J. Mater. Chem. A*, 2015, **3**, 21760–21771.

116 S. Draguta, O. Sharia, S. J. Yoon, M. C. Brennan, Y. V. Morozov, J. S. Manser, P. V. Kamat, W. F. Schneider and M. Kuno, *Nat. Commun.*, 2017, **8**, 200.
117 P. Qin, J. Zhang, G. Yang, X. Yu and G. Li, *J. Mater. Chem. A*, 2019, **7**, 1824–1834.
118 A. J. Knight, A. D. Wright, J. B. Patel, D. P. McMeekin, H. J. Snaith, M. B. Johnston and L. M. Herz, *ACS Energy Lett.*, 2019, **4**, 75–84.
119 V. M. Caselli, Z. Wei, M. M. Ackermans, E. M. Hutter, B. Ehrler and T. J. Savenije, *ACS Energy Lett.*, 2020, **5**, 3821–3827.
120 W. Li, K. Zhao, H. Zhou, W. Yu, J. Zhu, Z. Hu and J. Chu, *J. Phys. D: Appl. Phys.*, 2018, **52**, 045103.
121 A. D. Wright, R. L. Milot, G. E. Eperon, H. J. Snaith, M. B. Johnston and L. M. Herz, *Adv. Funct. Mater.*, 2017, **27**, 1700860.
122 T. Leijtens, G. E. Eperon, N. K. Noel, S. N. Habisreutinger, A. Petrozza and H. J. Snaith, *Adv. Energy Mater.*, 2015, **5**, 1500963.
123 H. J. Snaith, A. Abate, J. M. Ball, G. E. Eperon, T. Leijtens, N. K. Noel, S. D. Stranks, J. T.-W. Wang, K. Wojciechowski and W. Zhang, *J. Phys. Chem. Lett.*, 2014, **5**, 1511–1515.
124 E. L. Unger, E. T. Hoke, C. D. Bailie, W. H. Nguyen, A. R. Bowring, T. Heumüller, M. G. Christoforo and M. D. McGehee, *Energy Environ. Sci.*, 2014, **7**, 3690–3698.
125 Y. Gao, G. Walters, Y. Qin, B. Chen, Y. Min, A. Seifitokaldani, B. Sun, P. Todorovic, M. I. Saidaminov, A. Lough, S. Tongay, S. Hoogland and E. H. Sargent, *Adv. Mater.*, 2019, **31**, 1808336.
126 Y. Gao, X. Li, W. Liu, X. Xing, H. Long, K. Wang, B. Wang and P. Lu, *Nano Lett.*, 2021, **21**, 10230–10237.
127 T. Handa, D. M. Tex, A. Shimazaki, T. Aharen, A. Wakamiya and Y. Kanemitsu, *Opt. Express*, 2016, **24**, A917–A924.
128 W. A. Saidi and A. Kachmar, *J. Phys. Chem. Lett.*, 2018, **9**, 7090–7097.
129 W. Tan, A. R. Bowring, A. C. Meng, M. D. McGehee and P. C. McIntyre, *ACS Appl. Mater. Interfaces*, 2018, **10**, 5485–5491.
130 A. J. Barker, A. Sadhanala, F. Deschler, M. Gandini, S. P. Senanayak, P. M. Pearce, E. Mosconi, A. J. Pearson, Y. Wu, A. R. S. Kandada, T. Leijtens, F. De Angelis, S. E. Dutton, A. Petrozza and R. H. Friend, *ACS Energy Lett.*, 2017, **2**, 1416–1424.
131 L. Wang, J. J. Yoo, T.-A. Lin, C. F. Perkinson, Y. Lu, M. A. Baldo and M. G. Bawendi, *Adv. Mater.*, 2021, **33**, 2100854.
132 K. Prashanthan, B. Naydenov, K. Lips, E. Unger and R. W. MacQueen, *J. Chem. Phys.*, 2020, **153**, 164711.
133 A. S. Bieber, Z. A. VanOrman, S. Wieghold and L. Nienhaus, *J. Chem. Phys.*, 2020, **153**, 084703.
134 P. Zhao, B. J. Kim, X. Ren, D. G. Lee, G. J. Bang, J. B. Jeon, W. B. Kim and H. S. Jung, *Adv. Mater.*, 2018, **30**, 1802763.
135 S. Paek, P. Schouwink, E. N. Athanasopoulou, K. T. Cho, G. Grancini, Y. Lee, Y. Zhang, F. Stellacci, M. K. Nazeeruddin and P. Gao, *Chem. Mater.*, 2017, **29**, 3490–3498.
136 Y. Zhou, M. Yang, O. S. Game, W. Wu, J. Kwun, M. A. Strauss, Y. Yan, J. Huang, K. Zhu and N. P. Padture, *ACS Appl. Mater. Interfaces*, 2016, **8**, 2232–2237.
137 M. Xiao, F. Huang, W. Huang, Y. Dkhissi, Y. Zhu, J. Etheridge, A. Gray-Weale, U. Bach, Y.-B. Cheng and L. Spiccia, *Angew. Chem., Int. Ed.*, 2014, **53**, 9898–9903.
138 J. Li, P. Du, S. Li, J. Liu, M. Zhu, Z. Tan, M. Hu, J. Luo, D. Guo, L. Ma, Z. Nie, Y. Ma, L. Gao, G. Niu and J. Tang, *Adv. Funct. Mater.*, 2019, **29**, 1903607.
139 N. J. Jeon, J. H. Noh, Y. C. Kim, W. S. Yang, S. Ryu and S. I. Seok, *Nat. Mater.*, 2014, **13**, 897–903.
140 N. Lin, J. Qiao, H. Dong, F. Ma and L. Wang, *J. Mater. Chem. A*, 2015, **3**, 22839–22845.
141 S. Wieghold, A. S. Bieber, J. Lackner, K. Nienhaus, G. U. Nienhaus and L. Nienhaus, *ChemPhotoChem*, 2020, **4**, 704–712.
142 L. Nienhaus, J.-P. Correa-Baena, S. Wieghold, M. Einzinger, T.-A. Lin, K. E. Shulenberger, N. D. Klein, M. Wu, V. Bulović, T. Buonassisi, M. A. Baldo and M. G. Bawendi, *ACS Energy Lett.*, 2019, **4**, 888–895.
143 L. Wang, J. J. Yoo, T.-A. Lin, C. F. Perkinson, Y. Lu, M. A. Baldo and M. G. Bawendi, *Adv. Mater.*, 2021, **33**, 2100854.
144 C. M. Sullivan, A. S. Bieber, H. K. Drozdick, G. Moller, J. E. Kuszynski, Z. A. VanOrman, S. Wieghold, G. F. Strouse and L. Nienhaus, *Adv. Opt. Mater.*, 2022, 2201921.
145 A. D. Taylor, Q. Sun, K. P. Goetz, Q. An, T. Schramm, Y. Hofstetter, M. Litterst, F. Paulus and Y. Vaynzof, *Nat. Commun.*, 2021, **12**, 1878.
146 W. Zhang, S. Pathak, N. Sakai, T. Stergiopoulos, P. K. Nayak, N. K. Noel, A. A. Haghighirad, V. M. Burlakov, D. W. deQuilettes, A. Sadhanala, W. Li, L. Wang, D. S. Ginger, R. H. Friend and H. J. Snaith, *Nat. Commun.*, 2015, **6**, 10030.
147 S. Chen, X. Xiao, H. Gu and J. Huang, *Sci. Adv.*, 2021, **7**, eabe8130.
148 P. S. Mathew, G. F. Samu, C. Janáky and P. V. Kamat, *ACS Energy Lett.*, 2020, **5**, 1872–1880.
149 J. T. DuBose and P. V. Kamat, *Acc. Mater. Res.*, 2022, **3**, 761–771.
150 S. Wieghold, N. Shirato, V. Rose and L. Nienhaus, *J. Appl. Phys.*, 2020, **128**, 125303.
151 Y.-F. Chen, Y.-T. Tsai, D. M. Bassani, R. Clerc, D. Forgács, H. J. Bolink, M. Wussler, W. Jaegermann, G. Wantz and L. Hirsch, *J. Mater. Chem.*, 2016, **4**, 17529–17536.
152 M. Daboczi, S. R. Ratnasingham, L. Mohan, C. Pu, I. Hamilton, Y.-C. Chin, M. A. McLachlan and J.-S. Kim, *ACS Energy Lett.*, 2021, **6**, 3970–3981.
153 C. Das, M. Kedia, W. Zuo, C. Mortan, M. Kot, J. I. Flege and M. Saliba, *Sol. RRL*, 2022, **6**, 2200348.
154 C.-S. Li, T.-C. Cheng, S.-W. Shen, Y.-T. Wu, J.-R. Cheng, I.-C. Ni, M.-H. Chen and C.-I. Wu, *J. Phys. Chem. C*, 2019, **123**, 28668–28676.

155 R. E. Merrifield, *J. Chem. Phys.*, 1968, **48**, 4318–4319.
156 R. E. Merrifield, P. Avakian and R. P. Groff, *Chem. Phys. Lett.*, 1969, **3**, 155–157.
157 A. Suna, *Phys. Rev. B: Solid State*, 1970, **1**, 1716–1739.
158 P. W. Atkins and G. T. Evans, *Mol. Phys.*, 1975, **29**, 921–935.
159 C. Zhang, D. Sun, C.-X. Sheng, Y. X. Zhai, K. Mielczarek, A. Zakhidov and Z. V. Vardeny, *Nat. Phys.*, 2015, **11**, 427–434.
160 Y.-C. Hsiao, T. Wu, M. Li and B. Hu, *Adv. Mater.*, 2015, **27**, 2899–2906.
161 A. R. Bowman, S. D. Stranks and B. Monserrat, *Chem. Mater.*, 2022, **34**, 4865–4875.
162 C. A. Gueymard, *Sol. Energy*, 2004, **76**, 423–453.
163 T. A. Fasasi, C. M. Sin, L. Taili, S. W. Tsang and A. Ruotolo, *Opt. Mater.*, 2022, **124**, 112011.
164 S. Wieghold, A. S. Bieber, Z. A. VanOrman, A. Rodriguez and L. Nienhaus, *J. Phys. Chem. C*, 2020, **124**, 18132–18140.
165 E. Radiunas, L. Naimovičius, S. Raišys, A. Jozeliūnaitė, E. Orentas and K. Kazlauskas, *J. Mater. Chem. C*, 2022, **10**, 6314–6322.
166 S. Raišys, S. Juršėnas and K. Kazlauskas, *Sol. RRL*, 2022, **6**, 2100873.
167 Y. J. Bae, G. Kang, C. D. Malliakas, J. N. Nelson, J. Zhou, R. M. Young, Y.-L. Wu, R. P. Van Duyne, G. C. Schatz and M. R. Wasielewski, *J. Am. Chem. Soc.*, 2018, **140**, 15140–15144.
168 Y. J. Bae, J. A. Christensen, G. Kang, J. Zhou, R. M. Young, Y.-L. Wu, R. P. Van Duyne, G. C. Schatz and M. R. Wasielewski, *J. Chem. Phys.*, 2019, **151**, 044501.
169 T.-A. Lin, C. F. Perkinson and M. A. Baldo, *Adv. Mater.*, 2020, **32**, 1908175.
170 M. Einzinger, T. Wu, J. F. Kompalla, H. L. Smith, C. F. Perkinson, L. Nienhaus, S. Wieghold, D. N. Congreve, A. Kahn, M. G. Bawendi and M. A. Baldo, *Nature*, 2019, **571**, 90–94.
171 J. Hoche, H.-C. Schmitt, A. Humeniuk, I. Fischer, R. Mitrić and M. I. S. Röhr, *Phys. Chem. Chem. Phys.*, 2017, **19**, 25002–25015.
172 J. L. Bricks, Y. L. Slominskii, I. D. Panas and A. P. Demchenko, *Methods Appl. Fluoresc.*, 2017, **6**, 012001.
173 F. C. Spano and C. Silva, *Annu. Rev. Phys. Chem.*, 2014, **65**, 477–500.